

Accepted by the Astrophysical Journal, February 14th, 1999

EVIDENCE FOR PRESSURE DRIVEN FLOWS AND TURBULENT DISSIPATION IN THE SERPENS NW CLUSTER

Jonathan P. Williams^{1,2}

and

Philip C. Myers³

ABSTRACT

We have mapped the dense gas distribution and dynamics in the NW region of the Serpens molecular cloud in the CS(2–1) and N₂H⁺(1–0) lines and 3 mm continuum using the FCRAO telescope and BIMA interferometer. 7 continuum sources are found. The N₂H⁺ spectra are optically thin and fits to the 7 hyperfine components are used to determine the distribution of velocity dispersion. 8 cores, 2 with continuum sources, 6 without, lie at a local linewidth minimum and optical depth maximum. The CS spectra are optically thick and generally self-absorbed over the full 0.2 pc extent of the map. We use the line wings to trace outflows around at least 3, and possibly 4, of the continuum sources, and the asymmetry in the self-absorption as a diagnostic of relative motions between core centers and envelopes. The quiescent regions with low N₂H⁺ linewidth tend to have more asymmetric CS spectra than the spectra around the continuum sources indicating higher infall speeds. These regions have typical sizes ~ 5000 AU, linewidths ~ 0.5 km s⁻¹, and infall speeds ~ 0.05 km s⁻¹. The correlation of CS asymmetry with N₂H⁺ velocity dispersion suggests that the inward flows of material that build up pre-protostellar cores are driven at least partly by a pressure gradient rather than by gravity alone. We discuss a scenario for core formation and eventual star forming collapse through the dissipation of turbulence.

Subject headings: ISM: individual(Serpens) — ISM: kinematics and dynamics — stars: formation — turbulence

¹National Radio Astronomy Observatory, 949 N. Cherry Ave., Tucson AZ 85721

²Department of Astronomy, 211 Bryant Space Science Center, University of Florida, Gainesville, FL 32611; williams@astro.ufl.edu

³Harvard-Smithsonian Center for Astrophysics, 60 Garden Street, Cambridge, MA 02138; pmyers@cfa.harvard.edu

1. Introduction

Stars form through the collapse of dense cores within molecular clouds. The detection and measurement of the motions associated with such star forming collapse appears to be secure (see reviews by Evans 2000; Myers, Evans, & Ohashi 2000). The focus has primarily been on isolated, individual star forming regions since these are the least complex cases to understand both observationally and theoretically. However, the majority of stars form in clusters (Zinnecker, McCaughrean, & Wilking 1993) so a broader understanding of star formation, including such fundamental issues as the origin of the IMF and the formation of massive stars, requires the study of how stars form in groups.

Relative to an individual star, the deeper potential well of a stellar cluster should imply faster, and possibly easier to measure, inward motions, but observations are complicated by the generally greater distance to clusters than to individual star forming regions studied so far, and by the overpowering luminosity of massive stars that limit the ability to image lower mass neighbors and thus to obtain a complete view of cluster birth. For example, observations of the massive cluster forming region, W49N, have produced evidence for a global collapse of material onto the cluster as a whole (Welch et al. 1987) and, at higher resolution, for infall onto bright individual protostars (Zhang & Ho 1997). However, it has not been possible to explore the formation of more moderate mass stars in these objects because of dynamic range limitations.

In this paper, we present millimeter line and continuum observations of a cluster forming region in the Serpens molecular cloud. This region is well suited for an exploration into the formation processes of stellar clusters because it is nearby ($d=310$ pc; de Lara, Chavarria-K, & Lopez-Molina 1991) and contains a moderately dense embedded cluster (stellar density $\gtrsim 450$ pc $^{-3}$; Eiroa & Casali 1992) with many highly embedded millimeter wavelength continuum sources (Testi & Sargent 1998) but no O or B stars. In addition, Williams & Myers (1997) and Mardones (1998) have found signatures of widespread infall motions in this region.

The combination of proximity and low mass makes it possible to identify individual star forming condensations and examine the structure and dynamics of the cluster on a core by core basis. With this goal, we mapped the cluster in the optically thick CS(2–1) and thin N₂H⁺(1–0) lines with the FCRAO and BIMA telescopes. Their different optical depths allow us to probe cloud velocities from an outer envelope to the center (Leung & Brown 1977). The two species are also formed by different chemical pathways with abundances that depend on environment and time (Bergin et al. 1997) and thus their relative intensities offer information on the physical conditions and chemical age of the cores. In an earlier paper (Williams & Myers 1999a) we reported the discovery of a starless core that appears to be collapsing based on an analysis of a small part of the maps. Here, we report on the full dataset and investigate the dynamics of the dense gas across the whole cluster. We find a number of new cores, some starless, others with continuum sources, suggesting that new stars are continually being added to the group. There are spectroscopic signatures of outflow, infall, and localized dissipation of turbulence throughout the cloud which offer important clues about the

physical processes involved in cluster formation. The observations are outlined in §2 and the data displayed in §3. An analysis of the data follows in §4, and we discuss our findings in §5, concluding in §6.

2. Observations

Singledish maps of $\text{N}_2\text{H}^+(1-0)$ (93.1762650 GHz, $F_1F=01-12$) and $\text{CS}(2-1)$ (97.980968 GHz) were made at the Five College Radio Astronomy Observatory⁴ (FCRAO) 14 m telescope in December 1996 using the QUARRY 15 beam array receiver and the FAAS backend consisting of 15 autocorrelation spectrometers with 1024 channels set to an effective resolution of 24 kHz (0.06 km/s). The observations were taken in frequency switching mode and, after folding, 3rd order baselines were subtracted. The pointing and focus were checked every 3 hours on nearby SiO maser sources. The FWHM of the telescope beam is $50''$, and a map covering $6' \times 8'$ was made at Nyquist ($25''$) spacing. QUARRY was replaced with the SEQUOIA array in late 1997. This 16 element array is built with low noise MMIC based amplifiers and has much improved sensitivity. This enabled us to map the weak $\text{C}^{34}\text{S}(2-1)$ (96.412982 GHz) line using the same backends and observing technique in March 1998.

Observations were made with the 10 antenna Berkeley-Illinois-Maryland array⁵ (BIMA) for two 8 hour tracks in each line during April 1997 (CS; C array) and October/November 1997 (N_2H^+ ; B and C array). A two field mosaic was made with phase center, $\alpha(2000) = 18^{\text{h}}29^{\text{m}}47^{\text{s}}.5$, $\delta(2000) = 01^{\circ}16'51''.4$, centered close to S68N, and a second slightly overlapping pointing at $\Delta\alpha = 33''.0$, $\Delta\delta = -91''.0$, centered close to SMM1. Amplitude and phase were calibrated using 4 minute observations of 1751+096 (4.4 Jy) interleaved with each 22 minute integration on source. The correlator was configured with two sets of 256 channels at a bandwidth of 12.5 MHz (0.16 km s⁻¹ per channel) in each sideband and a total continuum bandwidth of 800 MHz.

The data were calibrated and maps produced using standard procedures in the MIRIAD package. The two pointings were calibrated together but inverted from the uv plane individually to avoid aliasing since their centers are separated by more than one primary beam FWHM. The FCRAO data (after first scaling to common flux units using a gain of 43.7 Jy K⁻¹) were then combined with the BIMA data using maximum entropy deconvolution. The final maps were produced by linearly mosaicking the two pointings in the xy plane. The combination of the single dish and interferometer data results in maps that are fully sampled from the map size down to the resolution limit (i.e., there is no “missing flux”).

⁴FCRAO is supported in part by the National Science Foundation under grant AST9420159 and is operated with permission of the Metropolitan District Commission, Commonwealth of Massachusetts

⁵Operated by the University of California at Berkeley, the University of Illinois, and the University of Maryland, with support from the National Science Foundation

In addition, we obtained a map of continuum emission by summing over the line-free channels. This map showed a number of point sources corresponding to warm dusty envelopes around embedded protostars. A similar map was obtained, over the entire Serpens complex, using the OVRO interferometer by Testi & Sargent (1998). Our map was of lower sensitivity and in order to make a better comparison, we were awarded additional time from February to April 1999 to map the continuum at 110 GHz in a mosaic consisting of 3 fields overlapping at their primary beam FWHM over the same region.

The resolution of the final (naturally weighted) maps was $8''.1 \times 5''.6$ at p.a. $+2^\circ$ for the continuum, $10''.0 \times 7''.8$ at p.a. -72° for CS, and $8''.5 \times 4''.6$ at p.a. $+2^\circ$ for N_2H^+ . Additional spectral line datasets were created by restoring to a common $10''$ (3100 AU) beam for analysis and comparison. The velocity resolution of these maps was 0.16 km s^{-1} .

3. Analysis

3.1. Continuum and integrated line maps

Maps of the continuum emission and integrated CS and N_2H^+ line intensities are presented in Figure 1. The continuum map was obtained from the 3 field mosaic at 110 GHz (see above). The rms noise level was $1.0 \text{ mJy beam}^{-1}$ at the center, increasing toward the map edges (all maps are corrected for primary beam attenuation). Seven sources are labeled; S68N, SMM1 (also known as S68 FIRS1), SMM5, and SMM10 were mapped by Casali, Eiroa, & Duncan (1993) and Davis et al. (1999) and we have labeled the three others S68Nb through S68Nd because of their proximity to S68N. These seven are also present in Testi & Sargent (1998) although we do not confirm several other sources in their map for which our data have sufficient coverage, sensitivity, and resolution to detect. Singledish observations with the 1.3 mm facility bolometer on the IRAM 30 m telescope should clarify the issue.

Source positions and fluxes are listed in Table 1. S68Nc may be a double or multiple source since it is highly elongated but we could not distinguish more than one significant peak, so it is listed in Table 1 as a single source. SMM1, with a peak flux of $165 \text{ mJy beam}^{-1}$, is considerably brighter than the other sources, and it proved problematic to clean the map completely of its sidelobes. Wright et al. (1999) pointed out that systematic errors including incomplete uv coverage, calibration uncertainties, and pointing errors, limit the fidelity of a mosaicked image to the true source brightness distribution to $1 - 2\%$ at best. Such errors would lie above the level of the noise and therefore may be misinterpreted as detections. Both clean and maximum entropy deconvolution methods (with varying parameters, and source modeling and replacement) produced maps that all contained the seven labeled sources but also created elongated features in the vicinity of SMM1 that varied in position and flux from map to map. Therefore we have a high confidence in the labeled sources in Figure 1 but we believe the unlabeled features to the southwest of SMM1 to be artifacts of the data acquisition and reduction process and we disregard them. The problems

associated with this map illustrate the difficulties in obtaining a complete view of cluster formation in more massive and luminous star forming environments.

There are also some image artifacts present in the line maps. The near-zero declination of the source resulted in strong north-south sidelobes even with the 45 baselines of the BIMA interferometer. As with the continuum map, these proved difficult to clean away completely and thus there may be some small sidelobe contamination from the brighter sources in each map. Based on experimenting with different deconvolution procedures, we estimate this uncertainty in line strengths to be 20% in addition to the thermal noise and flux calibration uncertainties.

The N_2H^+ and CS maps each show several condensations but present a very different appearance. The N_2H^+ map follows the distribution of the continuum sources much more closely than the CS map which features a prominent starless core to the west of S68N (Williams & Myers 1999a). These differences between the N_2H^+ and CS maps are probably due to a combination of differences in optical depth, protostellar outflows, and depletion. As we show below, the N_2H^+ emission is optically thin but most CS spectra are self-absorbed and have considerable optical depth. Moreover, outflow wings are prominent in the CS line profiles around SMM1 and S68N, but are almost entirely absent from the N_2H^+ spectra at the same positions. Finally, the time dependent chemical models of Bergin & Langer (1997) suggest that CS should deplete onto grains prior to star forming collapse but N_2H^+ should remain in the gas phase even at high densities during the collapse phase. For these reasons, in the following subsections we determine the physical properties of the cluster forming gas and individual star forming cores from the N_2H^+ data and measure motions between core envelopes and centers using the CS data.

3.2. $\text{N}_2\text{H}^+(1-0)$

The hyperfine structure of the $J = 1 - 0$ transition of N_2H^+ spreads out the emission into seven components (Caselli, Myers, & Thaddeus 1995), each with considerably lower intensity than a single component line would have, but with the benefit of also spreading out the optical depth so that individual components can be optically thin even when the sum of optical depths over all components might exceed unity. By fitting the seven hyperfine components simultaneously, we maximize the information in the data while taking advantage of the individual low optical depths to determine the systemic velocity and linewidth of the gas.

We fit the spectra using a function of the form,

$$T_{\text{B}}(v) = \left[J(T_{\text{ex}}) - J(T_{\text{bg}}) \right] \left\{ 1 - \exp\left[-\sum_i g_i \tau(v; v_i)\right] \right\}, \quad (1)$$

where the measured brightness temperature T_{B} is a function of velocity v , T_{ex} is the excitation temperature, $T_{\text{bg}} = 2.73$ K is the cosmic background temperature, and the sum is over hyperfine components $i = 1, 2, \dots, 7$. For each component, g_i is the statistical weight (Womack, Ziurys, & Wyckoff 1992) normalized so $\sum_i g_i = 1$, and $\tau(v; v_i)$ is the total optical depth parameterized by v_i ,

the relative centroid velocity of each component (Caselli et al. 1995),

$$\tau(v; v_i) = \tau_0 \exp[-(v - v_i - v_0)^2/2\sigma^2]. \quad (2)$$

Here τ_0 is the peak optical depth (summed over all components), v_0 is the systemic velocity of the gas, and σ is the velocity dispersion.

Spectra were analyzed across the map after first restoring to a circular $10''$ FWHM beam and sampling on a regular $10''$ square grid. The fits to the spectra require four parameters, T_{ex} , τ_0 , v_0 , and σ , but only the velocity and dispersion were tightly constrained by the data. The fitted excitation temperature and optical depth are determined from the intensities of the 7 hyperfine components but the two are inversely correlated resulting in a wide range of pairs that fit any given peak with only small changes in line shape that are indistinguishable given the moderate signal-to-noise ratios in the data. Moreover, there appear to be significant excitation anomalies analogous to the very low noise spectrum in Caselli et al. (1995). Because of the large uncertainties in T_{ex} and τ , we do not discuss them further.

We also made three component, optically thin, gaussian fits, $T_{\text{B}}(v) = T_0 \sum_i g_i \exp[-(v - v_i - v_0)^2/2\sigma^2]$, to the data. In most cases, the residuals were not significantly greater than the four parameter fit demonstrating the degeneracy in T_{ex} and τ . We also checked our fits with the hyperfine structure fitting routine in the CLASS data reduction package. All 3 methods show good agreement in the velocity and dispersion.

By adding synthetic noise to very low noise N_2H^+ spectra we tested the effect of varying signal-to-noise ratios on the fits. The systemic velocity could be accurately determined even in very noisy spectra but the fitted linewidth systematically increased as the signal-to-noise ratio decreased. The effect was noticeable for peak ratios less than 10, and became severe for ratios less than 5. In the following analysis, only spectra with peak signal-to-noise ratios greater than 5 are fit. For these spectra, we derived v_0 , and σ using the method described by equations (1) and (2).

The systemic velocity varies from 7.9 to 9.3 km s^{-1} and away from the outflow around S68N (see §3.3) there are no strong gradients. The dispersion displayed a more interesting variation. Figure 2 plots the non-thermal velocity dispersion, $\sigma_{\text{NT}} = [\sigma^2 - \sigma_{\text{T}}^2]^{1/2}$, where $\sigma_{\text{T}} = 0.075 \text{ km s}^{-1}$ is the thermal velocity dispersion for N_2H^+ at $T_{\text{kin}} = 20 \text{ K}$ (Wolf-Chase et al. 1998). The greatest values, $\sigma_{\text{NT}} > 0.6 \text{ km s}^{-1}$ occur in the cores containing the S68N and SMM1 sources which both power strong outflows. The minimum σ_{NT} is 0.16 km s^{-1} which is more than twice σ_{T} and shows that internal motions in the cores are predominantly turbulent. However, there are a number of regions where the turbulent velocity field drops to a local, confined, minimum. We identify eight such regions and label them Q1 through Q8 (for quiescent).

Three of the quiescent regions, Q1, Q2, and Q8, are coincident with peaks of integrated N_2H^+ intensity but the other five are not. Note that even in the low intensity regions, the signal-to-noise ratio is strong enough to determine the dispersion quite accurately and that any bias would tend to *increase* the dispersion. The quiescent regions are not prominent in the map of integrated intensity

because their linewidth is small. Indeed, our analysis of the data suggests to us that these quiescent “cores” are of greater interest than the cores of high integrated intensity.

The eight quiescent cores tend to have higher peak temperatures than their immediate surroundings and are especially prominent in Figure 3 which plots the peak N_2H^+ temperature divided by the total velocity dispersion. This is a measure of the optical depth (which was not well determined from the hyperfine fitting) and it rises toward the quiescent cores which possess both relatively low dispersion and high peak temperatures.

The quiescent core Q2 is almost coincident with the continuum source S68Nb and Q5 extends to encompass S68Nd but the other quiescent cores are apparently starless. Q6 lies $13''$ southeast of the strong CS core S68NW that was discussed in Williams & Myers (1999a). Table 2 lists the quiescent core locations, non-thermal velocity dispersion and the ratio of (thermal plus non-thermal) velocity dispersion as the data are smoothed from $10''$ to $50''$. This ratio is discussed later in §4 in the context of pressure gradients. Spectra toward the core centers at $15''$ and $50''$ resolution are shown in Figure 4. The $15''$ spectra are slightly smoothed from the highest available resolution so as to achieve a higher signal-to-noise ratio and more clearly show fine features in the spectral profiles. The lines are narrower and brighter at higher resolution and resemble the “kernels” in cluster forming cores described in Myers (1998). We discuss this point further in §4. The red shoulders in Q1, Q5, and Q8 are also apparent in the other hyperfine components and may simply be velocity structure or possibly self-absorption. None of the quiescent core spectra show blue shoulders from high velocity infall.

The concomitant decrease in velocity dispersion and increase in optical depth as measured by the peak temperature divided by the dispersion suggests that the quiescent cores have condensed out of the larger scale cluster forming cloud through a localized reduction in turbulent pressure support. The dissipation of turbulence as a means of core formation has been alluded to previously but has only recently been discussed explicitly by Nakano (1998) and Myers & Lazarian (1998). A decrease in pressure support should result in an inward flow of material. The search for such a flow is the subject of the following subsection.

3.3. CS(2–1)

A map of CS and $\text{C}^{34}\text{S}(2-1)$ spectra from FCRAO observations is shown in Figure 5. Since these two species share very similar chemical pathways, the differences in profiles are primarily due to their different optical depths. The ratio of peak CS to C^{34}S temperatures ranges from of 4–8 indicating moderate CS optical depths $\tau \simeq 1 - 3$ (Williams & Myers 1999b). Whereas the C^{34}S spectra present a single peak and are approximately gaussian, the CS spectra have low-level line wing emission and are generally double-peaked. The line wings are due to outflows from several cluster members, as we show below, and the two peaks result from self-absorption since the C^{34}S emission peaks at the dip of the CS spectra. Self-absorbed spectra from a static core would be

symmetric but here they are clearly asymmetric. We use the asymmetries in the self-absorption to probe the velocity differences between outer and inner regions of the cores, and thereby search for inward motions (e.g. Zhou 1995). A blue (low velocity) peak that is brighter than the red (high velocity) indicates that the (outer) absorbing layer is relatively red-shifted, i.e., infalling, whereas the opposite asymmetry implies outward motions. The greater the blue-red difference, the greater the relative motions between the inner and outer regions of the core (Myers et al. 1996).

There is a preponderance of spectra with infall-type asymmetry and only a few spectra around S68N with the opposite symmetry in Figure 5. Moreover, the average spectrum over the cluster (not shown) is self-absorbed with a brighter blue than red peak. This suggests that there is large scale contraction of the gas around the cluster. The size of the contracting region is greater than 0.2 pc in diameter and extends well beyond the continuum sources. Extended asymmetrical self-absorption in this source in the $2_{12} - 1_{10}$ line of H_2CO is also discussed in Mardones (1998). We have observed a similarly sized infalling region in CS(2–1) in the Cepheus A cluster forming region (Williams & Myers 1999b). At $50''$, the resolution of these data is too coarse to isolate the dynamics of individual cores but the addition of the interferometer maps allows us to follow infall and outflow motions down to the scale of the individual protostellar cores.

The Serpens cloud is known to contain a number of molecular outflows (White, Casali, & Eiroa 1995; Davis et al. 1999). Figure 6 maps the blue- and red-shifted emission for the BIMA data only. By analyzing the data prior to combining with the FCRAO data, the bulk of the mostly uniform cloud emission is resolved out and small scale features, such as outflows, stand out. The resulting map shows outflows around S68N, SMM1, SMM10, and possibly S68Nb. The existence of an outflow from S68Nb is uncertain because of confusion with the extensive red lobe around S68N.

CS spectra toward the quiescent cores and continuum sources are plotted in Figure 7. Here, we use the combined FCRAO/BIMA dataset since it is essential that all there be no missing flux if we are to interpret the spectra correctly. Spectra are centered on the position of minimum N_2H^+ linewidth for the quiescent cores or the continuum source otherwise, and are at a slightly smoothed $15''$ resolution. There are approximately symmetric line wings from the S68N, SMM1, and SMM10 outflows, a blue line wing from the possible outflow around Q2/S68Nb, and weak one-sided wings from the red lobe of the S68N outflow around Q5/S68Nd and Q7. The N_2H^+ velocity and FWHM linewidth are indicated by the solid vertical line and shading respectively (spectra are shown in Figure 4). The N_2H^+ velocity lies at the dip of the double-peaked CS spectra as for the C^{34}S spectra in Figure 5 except for Q8.

The Q8 core, with the narrowest N_2H^+ linewidth in the map, lies at the edge of the cluster and is uncontaminated by CS outflow wings. The CS spectra around the core all have the classic infall profile, but at the position of the linewidth minimum the N_2H^+ velocity lines up with the blue CS peak and not the dip as would be expected for self-absorption. Given that all the other double-peaked spectra in the map are self-absorbed it seems unlikely that the double-peaked spectra in this region are not also self-absorbed. However, the central N_2H^+ spectrum in Figure 4 shows a second,

red, peak at $15''$ and a red shoulder at $50''$ and it may be that the N_2H^+ is also self-absorbed here. The low resolution C^{34}S data in Figure 5 demonstrates that the CS spectra are self-absorbed in this region but to settle the issue in the Q8 core itself, sensitive higher resolution observations of C^{34}S are necessary.

Aside from the uncertainty over the interpretation of the Q8 core, Figure 7 shows an overall trend for the CS infall asymmetry to be greatest in those cores with small N_2H^+ linewidths. That is, the CS spectra toward the quiescent cores all have a greater blue than red peak indicating a positive infall velocity, but cores S68Nc, SMM10, and SMM1 present a very symmetric appearance indicating near-zero infall. The extended red CS outflow lobe from S68N in Figure 6 makes it difficult to isolate the Q5/S68Nd and Q7 cores and study their dynamics individually in this line, even though they are well separated in the N_2H^+ map. It is particularly difficult to diagnose infall motions around S68N itself where the infall asymmetry abruptly reverses from one position to another $10''$ away. Nevertheless, Figure 7 suggests a connection between the level of core turbulence and the asymmetry of the CS profiles, in turn related to the infall speed. We explore this in more detail in the following section.

4. Pressure driven flows and turbulent dissipation

The singledish spectra in Figure 5 suggests a global infall onto the cluster but the addition of the interferometer data allows a higher resolution view that reveal a wide range of spectral asymmetries that present a patchwork of inward and outward flows. The size of the region over which infall motions are observed is large, ~ 0.2 pc in diameter, at least partly because the cluster contains a number of collapsing cores. The (~ 3000 AU) resolution of the combined dataset separates out the individual protostars and protostellar cores from each other, and permits an analysis of how the small scale inward and outward motions are related to the local environment.

Detailed modeling of line profiles enable the infall speed to be determined (e.g., Zhou 1995; Williams et al. 1999) in isolated, low mass star forming cores but there is a much greater range of spectral shapes in the CS data here. For example, many are contaminated by outflows, either internal or overlapping from neighboring sources. Thus the modeling requires several additional parameters with the result that the uncertainty in the determination of the infall speed at each point is large. Therefore, rather than try to fit the spectra directly, we estimated the location of the main features in the CS spectra by eye using a simple cursor based routine. This resulted in a catalog of positions and velocities where the CS spectra have local peaks and dips.

The simplest estimate of the CS spectral asymmetry is the difference in blue and red peak temperatures, $\Delta T_{\text{b-r}} = T_{\text{blue}} - T_{\text{red}}$. We consider the difference, rather than the ratio of peak temperatures since it is determined with a smaller error. This is obviously only defined for double-peaked spectra and we therefore exclude spectra with possible infall “shoulders”. A second measure of asymmetry that has the advantage of being defined for all spectral shapes is the velocity difference

between the peak CS and N_2H^+ velocities. This is the unnormalized δv parameter introduced by Mardones et al. (1997). Based on simulations with simple two-layer infall models (Myers et al. 1996), we find that the blue-red temperature difference correlates linearly with the infall speed for a given optical depth and excitation temperature and that the scatter when a range of optical depths $\tau = 2 - 5$ and excitation temperatures $T_{\text{ex}} = 15 - 25$ K is considered is relatively small. The velocity difference also correlates linearly with infall speed but is more sensitive to optical depth variations. Consequently we use $\Delta T_{\text{b-r}}$ as a measure of infall speed and analyze its distribution across the cluster.

To test the hypothesis made in the previous section that the CS asymmetries are large where the N_2H^+ velocity dispersion is small, we simply plot $\Delta T_{\text{b-r}}$ against $\sigma_{\text{NT}}(\text{N}_2\text{H}^+)$ in Figure 8. The points are very scattered and there is no significant correlation between the two quantities. However, when binned by σ_{NT} , the average $\Delta T_{\text{b-r}}$ is greater than zero (implying a positive infall velocity). Moreover, $\Delta T_{\text{b-r}} > 0$ K for *all* spectra with $\sigma_{\text{NT}} < 0.23$ km s⁻¹. The lack of direct correlation is because several different dynamical states have been grouped together. By selecting individual regions, we can isolate the different states.

Figure 9 plots the variation of CS asymmetry and N_2H^+ velocity dispersion against the distance from the center of a core for two quiescent cores and two continuum sources. A similar behavior is found in the other cores: the velocity dispersion tends to increase and the blue-red temperature difference generally decreases with increasing radius from the center of the quiescent cores and vice versa for the continuum sources. Moreover, the temperature difference is positive at the centers of the quiescent cores but is small or negative (i.e., outflow) at the centers of the continuum cores.

The slopes of the least squares fits, or the radial gradients, of the CS blue-red temperature difference and N_2H^+ non-thermal velocity dispersion are tabulated in Table 3 and plotted against each other in Figure 10. Generally, the quiescent cores lie toward the lower right section (increasing N_2H^+ dispersion and decreasing CS asymmetry with radius) and the continuum sources lie in the upper right section (decreasing N_2H^+ dispersion and increasing CS asymmetry with radius). For a constant density, a change in velocity dispersion implies a change in pressure which results in a flow toward the lower pressure (i.e., lower dispersion) regions. The conversion from CS asymmetry to infall speed depends not only on the blue-red temperature difference but also the excitation temperature and optical depth. If these do not vary greatly from core envelope to center then the observed increase in $\Delta T_{\text{b-r}}$ as σ_{NT} decreases toward the centers of the quiescent cores implies an increase in infall speed.

Since the pressure depends linearly on the density and quadratically on the velocity dispersion, and since the infall speed is more sensitive to the blue-red temperature difference than the excitation temperature and optical depth, the inverse correlation of $\Delta T_{\text{b-r}}$ with σ_{NT} in Figure 10 is evidence for pressure driven, inward, flows in the quiescent cores. The correlation also extends to negative dispersion gradients and outflow motions around the continuum sources illustrating the disruptive effect of young protostars on their parent cloud. Finally, we note that a fit through the data points

suggests a slightly negative CS asymmetry gradient at $d\sigma_{\text{NT}}/dr = 0$ which may indicate small, presumably gravitational, inward motions even when the pressure gradient is zero.

Using the two-layer model of Myers et al. (1996), we find that the infall speed corresponding to a typical value, $\Delta T_{\text{b-r}} = 1$ K, for $\sigma_{\text{NT}} = 0.3$ km s⁻¹ is $v_{\text{in}} \simeq 0.05$ km s⁻¹. This is quite small and similar to that expected for the quasistatic contraction of a magnetically supported, isothermal core (Lizano & Shu 1989). However, the nature of the flow is very different from the predictions of such ambipolar diffusion models: all the cores, whether with or without continuum sources, have highly non-thermal linewidths and the infall speed is greatest in those cores with the smallest linewidths. This inverse correlation is not expected in a purely gravitational collapse and is more suggestive of a pressure driven flow. Nakano (1998) and Myers & Lazarian (1998) describe how inward flows onto a core can occur through the dissipation of turbulence and consequent loss of pressure support. As a core grows and its center becomes more opaque to ionizing radiation, its coupling to the magnetic field, and the range of MHD waves that propagate through it, decrease. Without replenishment, the waves decay within a free-fall time and the turbulent pressure, $\rho\sigma_{\text{NT}}^2$, rapidly decreases (where ρ is the mass density). Since wave support is maintained in the lower opacity, more highly ionized, core envelope, its pressure remains the same with the result that there is a pressure gradient, leading to a flow, from core envelope to center. The magnitude of the flow will be greatest where the pressure gradient is greatest, or equivalently where the central linewidths are smallest if the external pressure is approximately constant.

The magnitude of the inward speed depends on the pressure difference between core center and envelope. The observed inward motions are small, $v_{\text{in}} \ll \sigma_{\text{NT}}$, and therefore the pressure differences are small. Since the total (thermal plus non-thermal) velocity dispersion at 10'' is a factor of 0.36 – 0.75 less than at 50'' (Table 2), the density contrast between core centers and envelopes is inferred to lie in the range 2 – 8. This is comparable to the ratio of peak to average density for cores in the Ophiuchus cluster forming cloud (Motte, André, & Neri 1998).

As the core grows, the opacity increases further until the ionization is dominated by cosmic rays ($A_V \simeq 4$; McKee 1989). In this case, Myers (1998) predicts the existence of “kernels”, ~ 6000 AU, in size that are completely cutoff from MHD waves. If the external pressure is sufficiently large, as in massive star forming regions, these kernels can be stable, supported by thermal pressure against their self-gravity. The criterion for stability (Myers 1998 equation 3) can be rewritten as $\sigma_{\text{NT}}/\sigma_{\text{T}} = 1.5$ which is satisfied in all the cores here where we have found $\sigma_{\text{NT}}/\sigma_{\text{T}} > 2.1$. The quiescent cores extend over 10'' – 20'', which is close to the expected size of a kernel, and their velocity FWHM are ~ 0.5 km s⁻¹ similar to Myers’ Figure 2, but there is insufficient signal-to-noise to discern the predicted thermal “spike”. There are possible examples in the residuals to the hyperfine fits to the spectra but they are not consistent across all the components and may be due to poorly cleaned sidelobes from other cores (the cleaning method is non-linear and varies in its effectiveness from channel to channel). High spatial and velocity resolution singledish observations of higher transition lines such as N₂H⁺(3–2) offer an independent test for the presence of a thermal spike and may also be used to constrain the density contrast in the cores.

The maps in Figures 1,2 reveal a number of protostars and pre-protostellar collapsing cores. The cluster did not form in a single event, therefore, but continues to accrue members through an ongoing process of individual star formation. Hurt & Barsony (1996) analyzed the spectral energy distribution (SED) of several of the bright sources in this cluster and concluded that they were Class 0 protostars. The IRAS data does not have the resolution to resolve the emission (and therefore to define their SED in the far-infrared) from the seven continuum sources that we have identified here but if, following Hurt & Barsony, we divide up the IRAS fluxes evenly between all the objects, all seven would be classified as Class 0.

The discovery of the quiescent cores, and their association with high infall motions, suggests that they are the precursors to the Class 0 sources. Within the boundaries of the maps here, and at the sensitivity of the observations, we have found approximately equal numbers of continuum sources and quiescent cores (7 and 8 respectively, with 2 shared). If stars continue to form at a constant rate, then the lifetime of the quiescent cores must be approximately the same as the lifetime of the Class 0 phase of protostellar evolution, $\sim 3 \times 10^4$ yr (André & Montmerle 1994). Such a short lifetime implies a dynamic evolution since the free-fall timescale, $t_{\text{ff}} = (G\rho)^{-1/2} \simeq 6 \times 10^4$ yr, for $n_{\text{H}_2} = 10^6 \text{ cm}^{-3}$, approximately equal to the inferred volume density of the quiescent cores and a factor of two greater than the critical density of N_2H^+ . This rapid evolution is consistent with core growth through the decay of turbulence since this should occur on a free-fall timescale (Nakano 1998).

5. Summary

This paper presents millimeter wavelength continuum and spectral line observations of a young, embedded, low mass cluster forming region in the Serpens molecular cloud. 7 continuum sources are found at the resolution and sensitivity of these data. The distribution of these sources corresponds well with the N_2H^+ emission but the CS data presents a different appearance, with high velocity emission from outflows around 4 continuum sources, and central dips in spectral profiles from self-absorption (as shown on the large scale from singledish C^{34}S data and on the small scale from the N_2H^+). Away from the powerful outflow around S68N, the self-absorption is red-shifted which we interpret as indicating inward motions.

The N_2H^+ linewidth is dominated by non-thermal motions throughout the cluster. However, there are 8 regions where the non-thermal velocity dispersion reaches a local minimum. 6 are starless and 2 contain continuum sources. They do not all coincide with peaks of the integrated intensity but they all stand out in maps of the peak temperature divided by the dispersion, a measure of the optical depth. The CS spectra toward these “quiescent” cores are particularly asymmetric, indicating relatively high infall speeds. Generally, the N_2H^+ dispersion increases and the CS blue-red temperature difference decreases with increasing distance from the core centers, and vice versa for the continuum sources. The correlation of CS asymmetry, related to infall speed, with N_2H^+ dispersion, related to the local turbulent pressure, suggests that the inward flows are at least

partly pressure driven and that the cores formed through the localized dissipation of turbulence as envisioned by Nakano (1998) and Myers & Lazarian (1998). Such a scenario is consistent with the observed numbers of quiescent cores and Class 0 sources.

The singledish data alone shows a net inward motion onto the cluster. Although there is clearly considerable smearing of the detailed dynamics, this suggests that it may be fruitful to search for infall signatures in more distant clusters at $\sim 0.1 - 0.2$ pc resolution. It will, of course, be important to observe other nearby cluster forming regions at higher resolution, $\lesssim 3000$ AU, to augment this study. Ultimately, the comparison of conditions in many clusters will give a clearer picture of their formation, show the effects of different environments, and, through an inventory of continuum sources and pre-protostellar cores, can be hoped to elucidate the origins of the stellar IMF (Motte et al. 1998; Testi & Sargent 1998).

JPW is supported by a Jansky fellowship. Partial support has also been provided by the NASA Origins of Solar Systems Program, grant NAGW-3401. We thank Leo Blitz and Dick Plambeck for generously assigning additional BIMA tracks to remap the continuum emission and Marc Pound and Tamara Helfer for advice concerning the data reduction.

REFERENCES

- André, P. & Montmerle, T. 1994, *ApJ*, 420, 837
Bergin, E.A., Goldsmith, P.F., Snell, R.L., & Langer, W.D. 1997, *ApJ*, 482, 285
Bergin, E.A., & Langer, W.D. 1997, *ApJ*, 486, 316
Casali, M.M., Eiroa, C., & Duncan, W.D. 1993, *A&A*, 275, 195
Caselli, P., Myers P.C., & Thaddeus, P. 1995, *ApJ*, 455, L77
Davis, C.J., Matthews, H.E., Ray, T.P., Dent, W.R.F., & Richer, J.S. 1999, *MNRAS*, in press
Eiroa, C., & Casali M.M. 1992, *A&A*, 262, 468
Evans, N.J.II 2000, *ARA&A*, in press
Hurt, R.L., & Barsony, M. 1996, *ApJ*, 460, L45
de Lara, E., Chavarría-K, C., & Lopez-Molina, G. 1991, *A&A*, 243, 139
Leung, C.M., & Brown, R.B. 1977, *ApJ*, 214, L73
Lizano, S., & Shu, F.H. 1989, *ApJ*, 342, 834
Mardones, D., Myers, P.C., Tafalla, M., Wilner, D.J., Bachiller, R., & Garay, G. 1997, *ApJ*, 489, 719
Mardones, D. 1998, Ph.D. Thesis, Harvard University
McKee, C.F. 1989, *ApJ*, 345, 782
Motte, F., André, Ph., & Neri, R. 1998, *A&A*, 336, 150
Myers, P.C., Evans, N.J.II, & Ohashi, N. 2000, in “Protostars and Planets IV”, ed. V. Mannings, A.P. Boss & S.S. Russell (Tucson: University of Arizona Press), in press
Myers, P.C., & Lazarian, A. 1999, *ApJ*, 507, L157
Myers, P.C. 1998, *ApJ*, 496, L109
Myers, P.C., Mardones, D., Tafalla, M., Williams, J.P., Wilner, D.J. 1996, *ApJ*, 465, L133

- Nakano, T. 1998, *ApJ*, 494, 587
- Testi, L., & Sargent, A.I. 1998, *ApJ*, 508, L91
- Ungerechts, H., Bergin, E.A., Goldsmith, P.F., Irvine, W.M., Schloerb, F.P., & Snell, R. L. 1997, *ApJ*, 482, 245
- Welch, W.J., Jackson, J.M., Dreher, J.W., Terebey, S., & Vogel, S.N 1987, *Science*, 238, 1550
- White, G.J., Casali, M.M., & Eiroa, C. 1995, *A&A*, 298, 594
- Williams, J.P., & Myers, P.C. 1999a, *ApJ*, 518, L37
- Williams, J.P., & Myers, P.C. 1999b, *ApJ*, 511, 208
- Williams, J.P., Myers, P.C., Wilner, D.J., & Di Francesco, J. 1999, *ApJ*, 513, L61
- Williams, J.P., & Myers, P.C. 1997, in “Star Formation, Near and Far”, AIP Conference Proceedings 393, eds. S.S. Holt and L.G. Mundy, 387
- Wolf-Chase, G.A., Barsony, M., Wootten, H.A, Ward-Thompson, D., Lowrance, P.J., Kastner, J.H., & McMullin, J.P. 1998, 501, L193
- Womack, M., Ziurys, L.M., & Wyckoff, S. 1992, *ApJ*, 387, 417
- Wright, M.C.H., Dickel, J., Koralesky, B., & Rudnick, L. 1999, *ApJ*, 518, 284
- Zhang, Q., & Ho, P.T.P. 1997, *ApJ*, 488, 241
- Zhou S. 1995, *ApJ*, 442, 685
- Zinnecker, H., McCaughrean, M.J., & Wilking, B.A. 1993, in *Protostars and Planets III*, eds. E. Levy, J.I. Lunine, & M.S. Matthews (Tucson: U. of Arizona Press), 429

TABLE 1
Continuum Sources

Source	$\Delta\alpha^a$ (")	$\Delta\delta^a$ (")	Flux density (mJy)	Peak (mJy beam ⁻¹)
SMM1	34.1	-91.0	233.7	164.7
S68N	9.0	-7.8	36.1	20.2
S68Nd	23.0	-28.9	32.3	15.6
SMM10	66.9	-60.4	25.3	22.1
SMM5	56.4	-11.7	20.7	13.7
S68Nc ^b	18.7	7.5	20.4	12.1
S68Nb	30.6	19.4	17.7	15.1

^a location of peak relative to
 $\alpha(2000) = 18^{\text{h}}29^{\text{m}}47^{\text{s}}.5, \delta(2000) = 01^{\circ}16'51''.4$

^b possibly multiple sources

TABLE 2
Quiescent Cores

Core	$\Delta\alpha^a$ (")	$\Delta\delta^a$ (")	v_{LSR} (km s ⁻¹)	$\sigma_{\text{NT}} (10'')$ (km s ⁻¹)	$\frac{\sigma_{\text{tot}}(10'')}{\sigma_{\text{tot}}(50'')}$	$\frac{T_{\text{peak}}(10'')}{T_{\text{peak}}(50'')}$
Q1	17.4	39.0	8.482	0.17	0.52	2.9
Q2	28.2	18.6	8.757	0.20	0.68	1.7
Q3	41.4	-1.8	8.514	0.19	0.68	1.6
Q4	43.8	-18.6	8.353	0.21	0.69	1.4
Q5	15.0	-35.4	8.189	0.23	0.52	1.2
Q6	-42.6	-29.4	8.601	0.24	0.75	1.6
Q7	10.2	-66.6	8.311	0.20	0.52	1.1
Q8	83.4	-91.8	7.964	0.16	0.36	1.9

^a location of minimum σ_{NT} relative to
 $\alpha(2000) = 18^{\text{h}}29^{\text{m}}47^{\text{s}}.5, \delta(2000) = 01^{\circ}16'51''.4$

TABLE 3
Radial Gradients

Core	$d\Delta T_{b-r}/dr$ (K pc ⁻¹)	err	$d\sigma_{NT}/dr$ (km s ⁻¹ pc ⁻¹)	err
Q1	-12.2	9.7	-0.36	2.43
Q2/S68Nb	-11.1	18.5	5.52	2.74
Q3	-32.2	16.7	5.02	1.67
Q4	-23.7	17.3	4.87	1.38
Q5/S68Nd	-10.2	15.1	0.13	2.17
Q6	-49.4	20.2	6.69	2.97
Q7	-22.1	7.8	3.87	1.39
Q8	-19.5	8.0	9.05	1.69
SMM1	4.0	7.1	-2.71	1.51
S68N	62.7	16.6	-7.46	2.68
SMM10	28.8	7.2	-3.32	1.51
SMM5	-11.9	8.3	0.07	1.09
S68Nc	7.4	10.2	-1.54	2.27

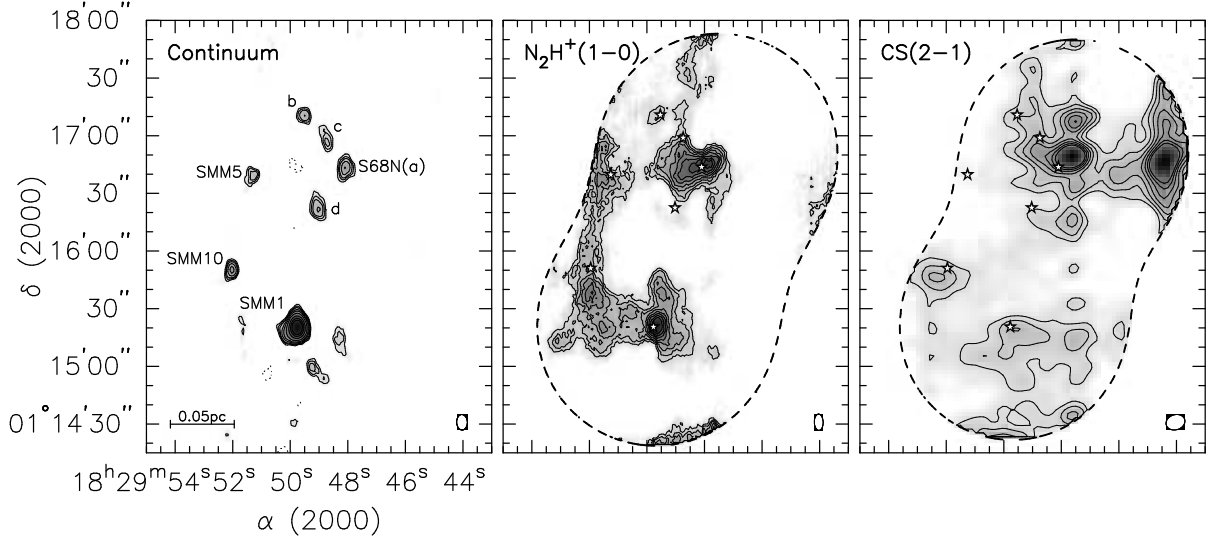


Fig. 1.— Continuum and line emission in the Serpens cluster. The left panel shows the continuum emission at 110 GHz in a logarithmic greyscale ranging from 5 to 200 mJy beam⁻¹, and contours at 7, 9, 11, 15, 20, 30, 50 mJy beam⁻¹ (dotted contours are their negative counterparts). The seven labeled sources (other objects are believed to be artifacts; see text) are indicated in the two other panels by the star-shaped symbols. The center panel shows the combined BIMA+FCRAO N₂H⁺(1-0) emission integrated over all hyperfine components from $v = 6.5$ to 10.0 km s⁻¹. The greyscale ranges linearly from 2.7 to 36 K km s⁻¹, with contours at 8.2, 10.9, 13.6, ...K km s⁻¹. The right panel shows the combined BIMA+FCRAO CS(2-1) emission integrated from $v = 0.75$ to 10.5 km s⁻¹. The greyscale ranges linearly from 5 to 40 K km s⁻¹, with contours at 10, 12.5, 15, ...K km s⁻¹. Both line maps have been corrected for primary beam attenuation and masked beyond the dotted boundaries corresponding to the 50% level of the two pointings. Synthesized beam sizes are indicated in the lower right corner for each map.

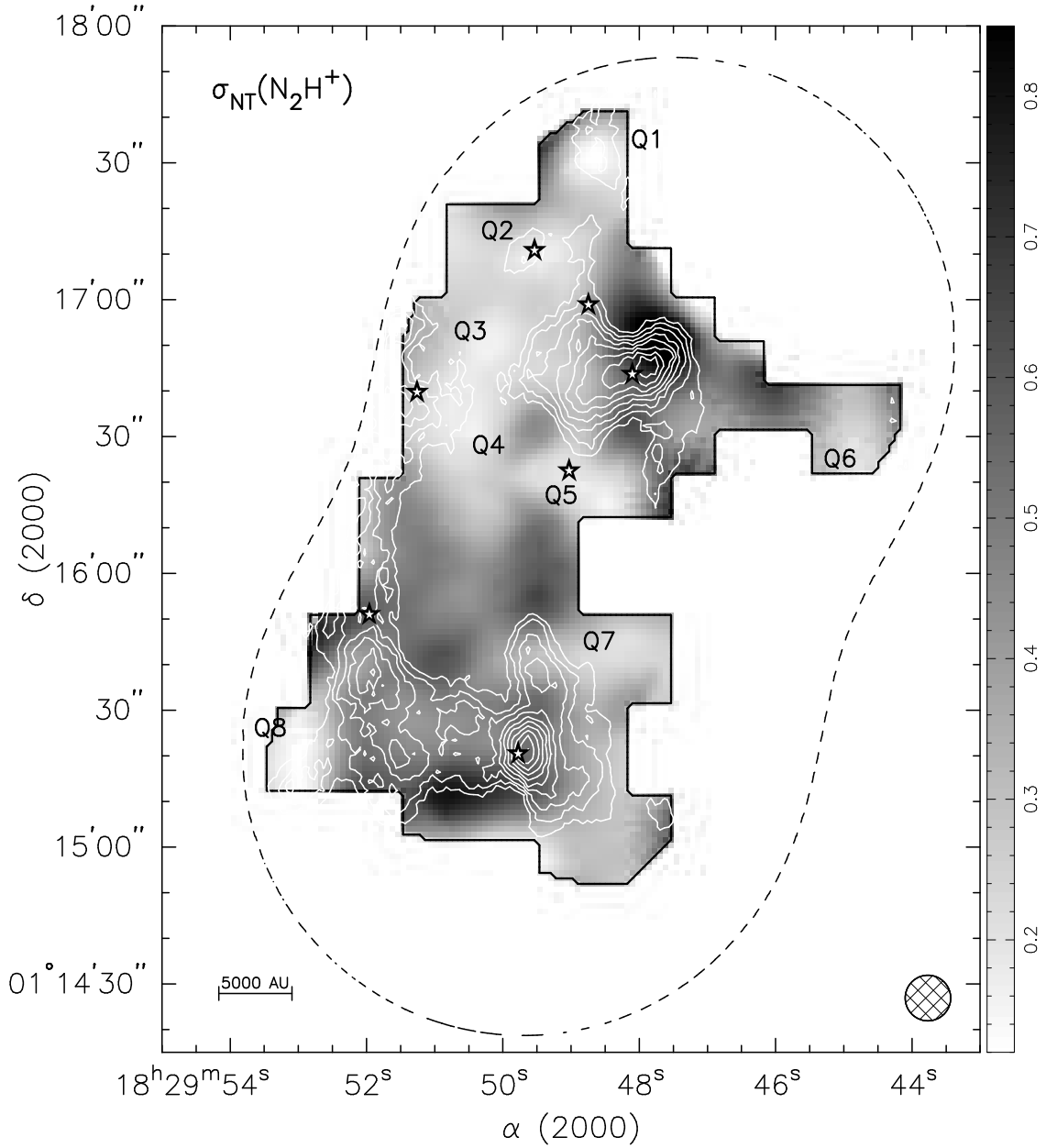


Fig. 2.— The non-thermal velocity dispersion of N_2H^+ displayed in greyscale overlaid on a contour map of integrated emission as in Figure 1. The dispersion was only determined for those spectra with a peak signal-to-noise ratio greater than 5 and lie within the boundary shown by the heavy solid line. The dashed line indicates the FWHM of the mosaic. The resolution of this map is $10''$ indicated in the lower right corner. We identify eight regions where the velocity dispersion is a local minimum, labeled Q1 through Q8.

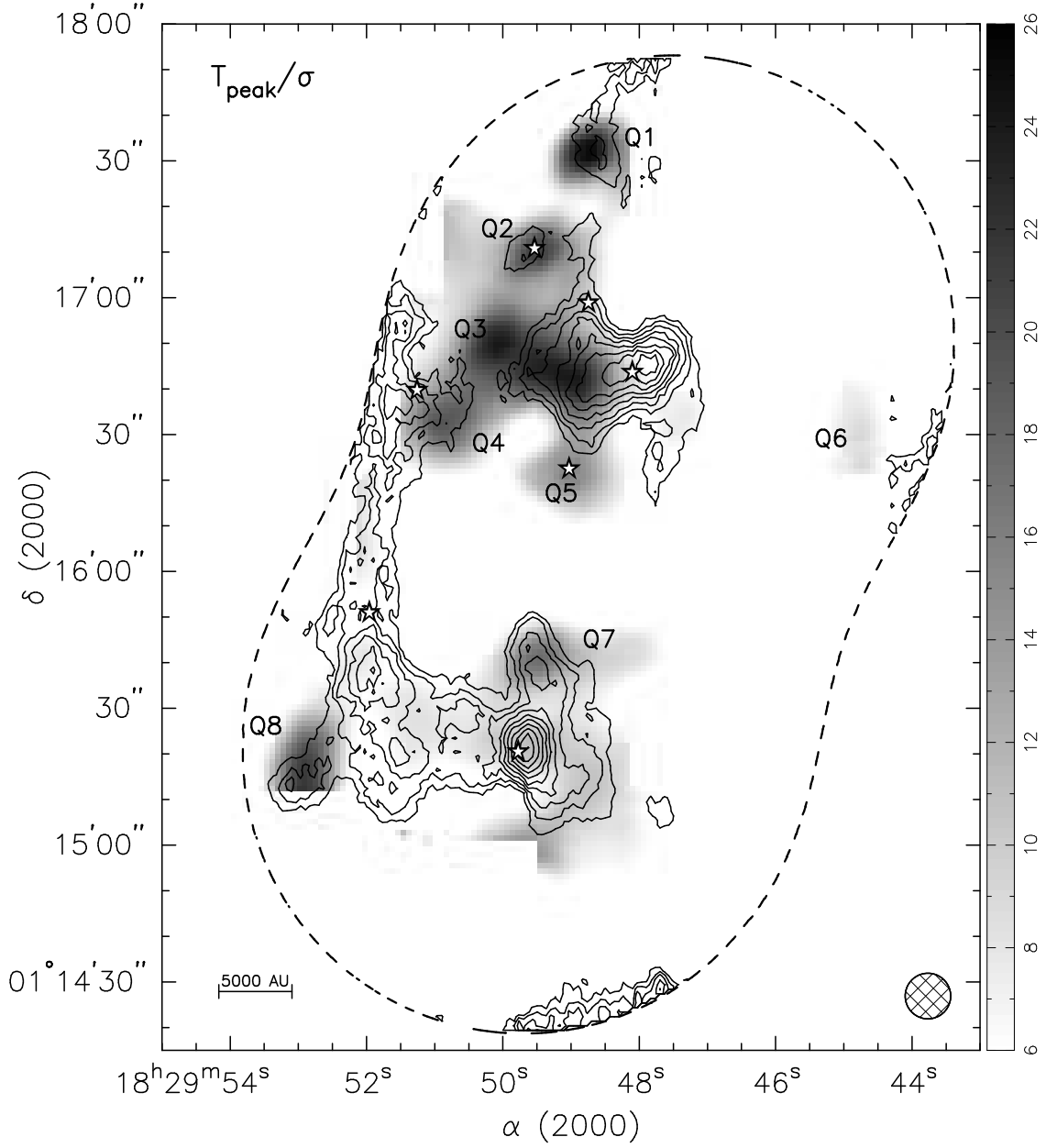


Fig. 3.— The peak temperature divided by the velocity dispersion for the N_2H^+ spectra, a measure of the optical depth, plotted in greyscale over a contour map of integrated emission. The greyscale ranges linearly from 6 to 24 $\text{K} (\text{km s}^{-1})^{-1}$. The boundary and annotations are as in Figure 2. The quiescent cores are most prominent in this map since they possess both a locally small dispersion and high peak temperature.

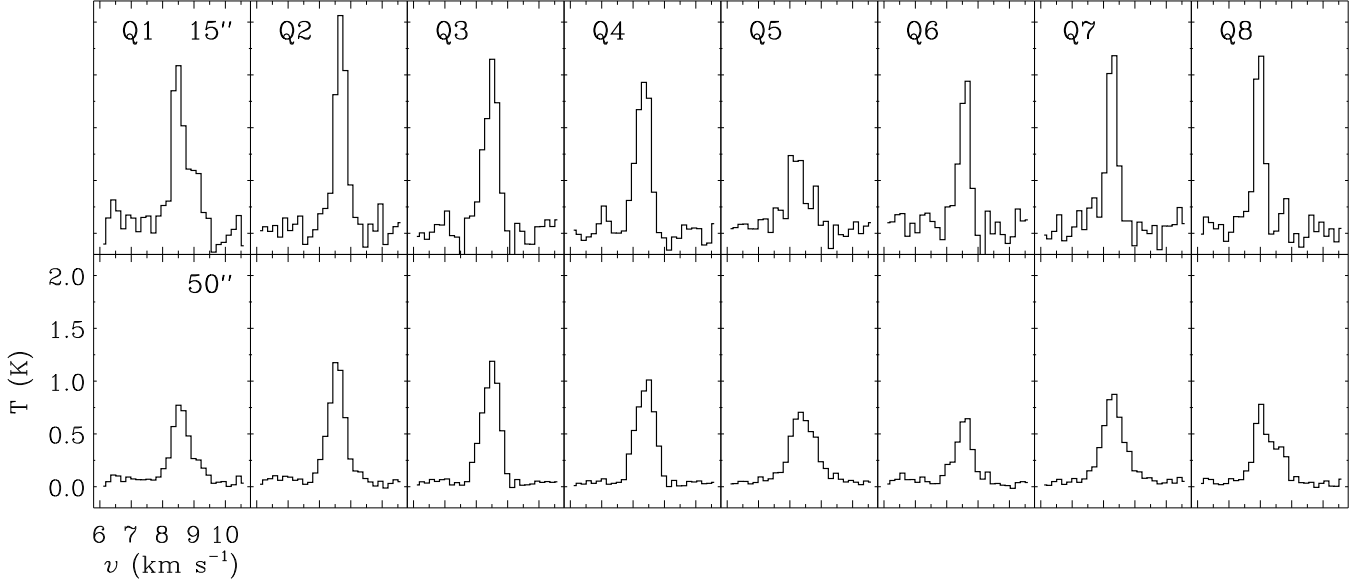


Fig. 4.— N_2H^+ spectra at the center of the 8 quiescent cores Q1–Q8. The upper panels show spectra at $15''$ resolution and the lower panels show spectra at the same positions at $50''$ resolution. Only the isolated ($F_1F=01-12$) hyperfine component is shown. The velocity and temperature scale is the same for all panels and is indicated in the lower left.

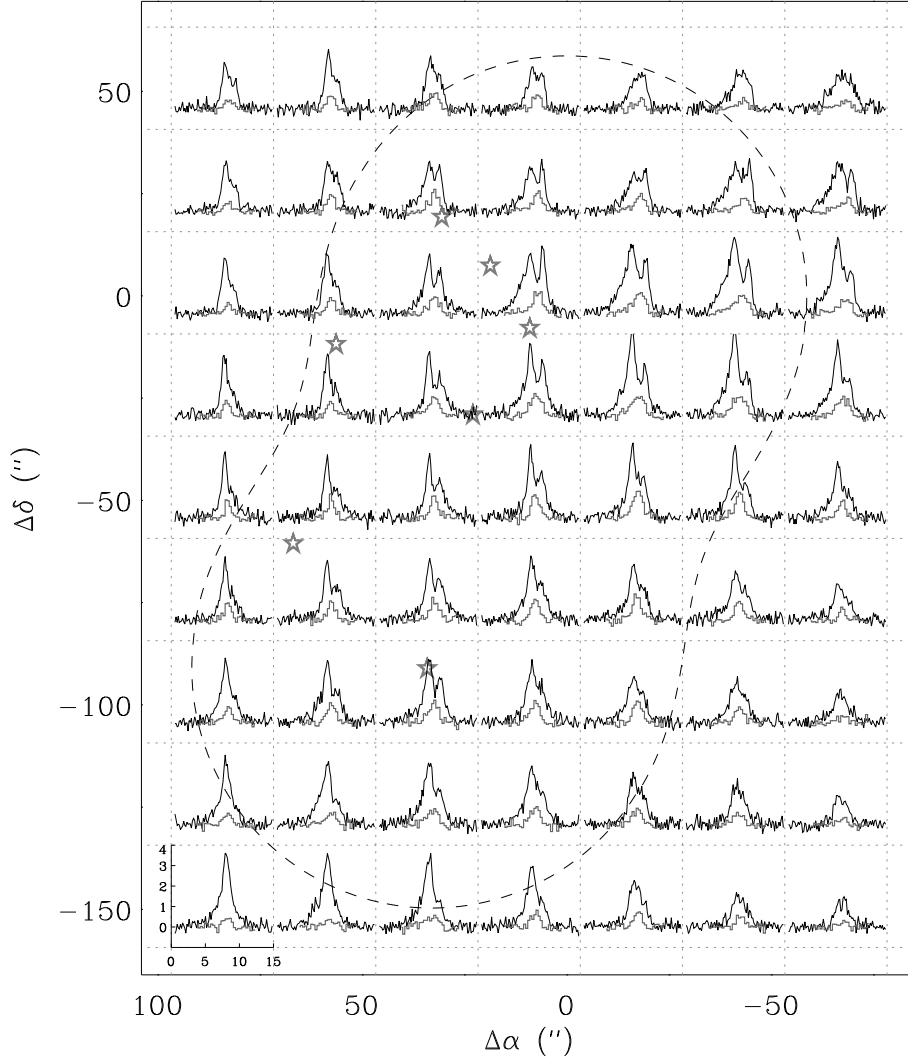


Fig. 5.— Map of CS and $C^{34}S(2-1)$ spectra from FCRAO observations (dark and light lines respectively). The $C^{34}S$ intensities have been multiplied by a factor of 2 for clarity. The spectra are placed on a (Nyquist) $25''$ grid with a velocity range 0 to 15 km s^{-1} and a temperature range -1 to 4 K (T_R^*) for each box shown by the dotted line and indicated by the axes for the lower left box. The outline of the BIMA CS map and the seven continuum sources from Figure 1 are indicated. Offset coordinates are relative to $\alpha(2000) = 18^{\text{h}}29^{\text{m}}47^{\text{s}}.5$, $\delta(2000) = 01^{\circ}16'51''.4$.

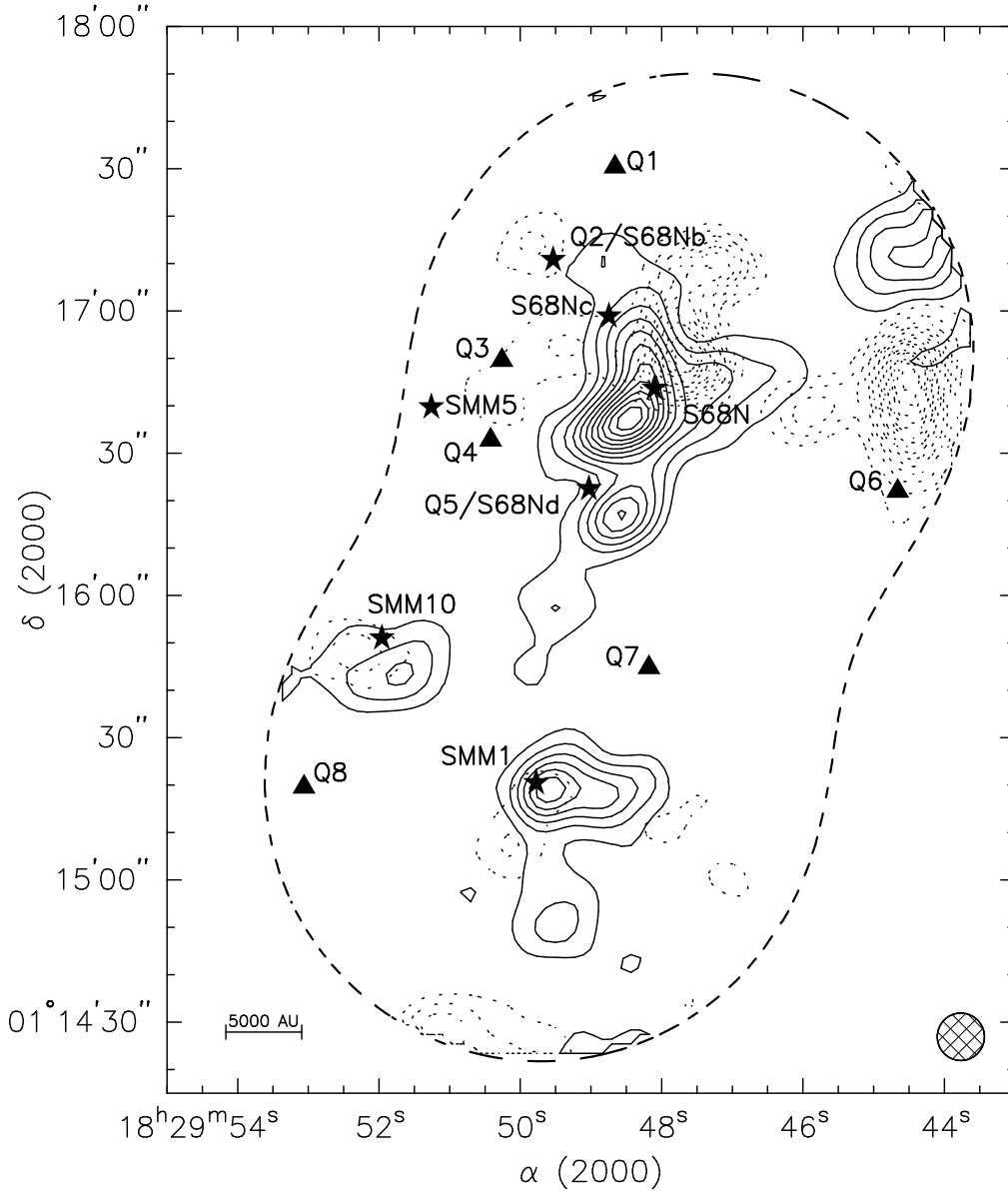


Fig. 6.— Blue- and red-shifted CS emission showing several protostellar outflows. The dotted contours show the integrated intensity from 5.75 to 6.75 km s^{-1} , the solid contours from 9.25 to 11.0 km s^{-1} . Starting level and increment is 0.5 K km s^{-1} in each case. The map is made using BIMA data only restored to a circular $10''$ FWHM beam indicated in the lower right corner. The locations of the continuum sources and quiescent cores are indicated by the star and triangle symbols respectively. The S68N outflow dominates and its red lobe extends across the Q5/S68Nd core. The SMM1 outflow is confined to a much smaller projected area and does not appear to be responsible for line wings around other cores. There is a weak outflow around continuum core SMM10, and hints of an outflow around Q2/S68Nb.

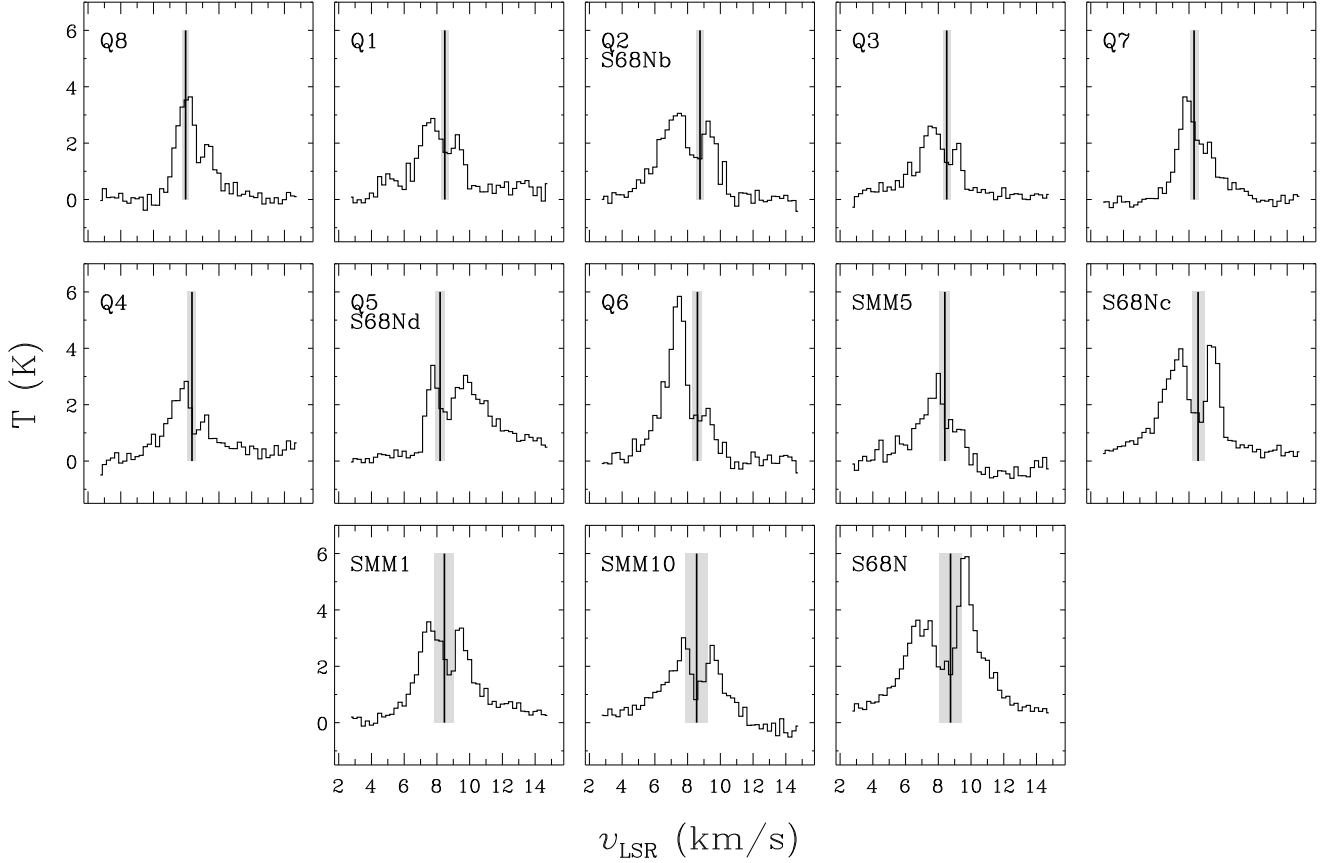


Fig. 7.— CS spectra toward the quiescent cores and continuum sources. Spectra have been slightly smoothed to $15''$ to better show the lineshapes. The velocity and temperature scale is the same for each spectrum. N_2H^+ velocities and FWHM linewidths are indicated by the solid vertical line and gray shading respectively; spectra are ordered from lowest (top left) to highest (bottom right) N_2H^+ linewidth.

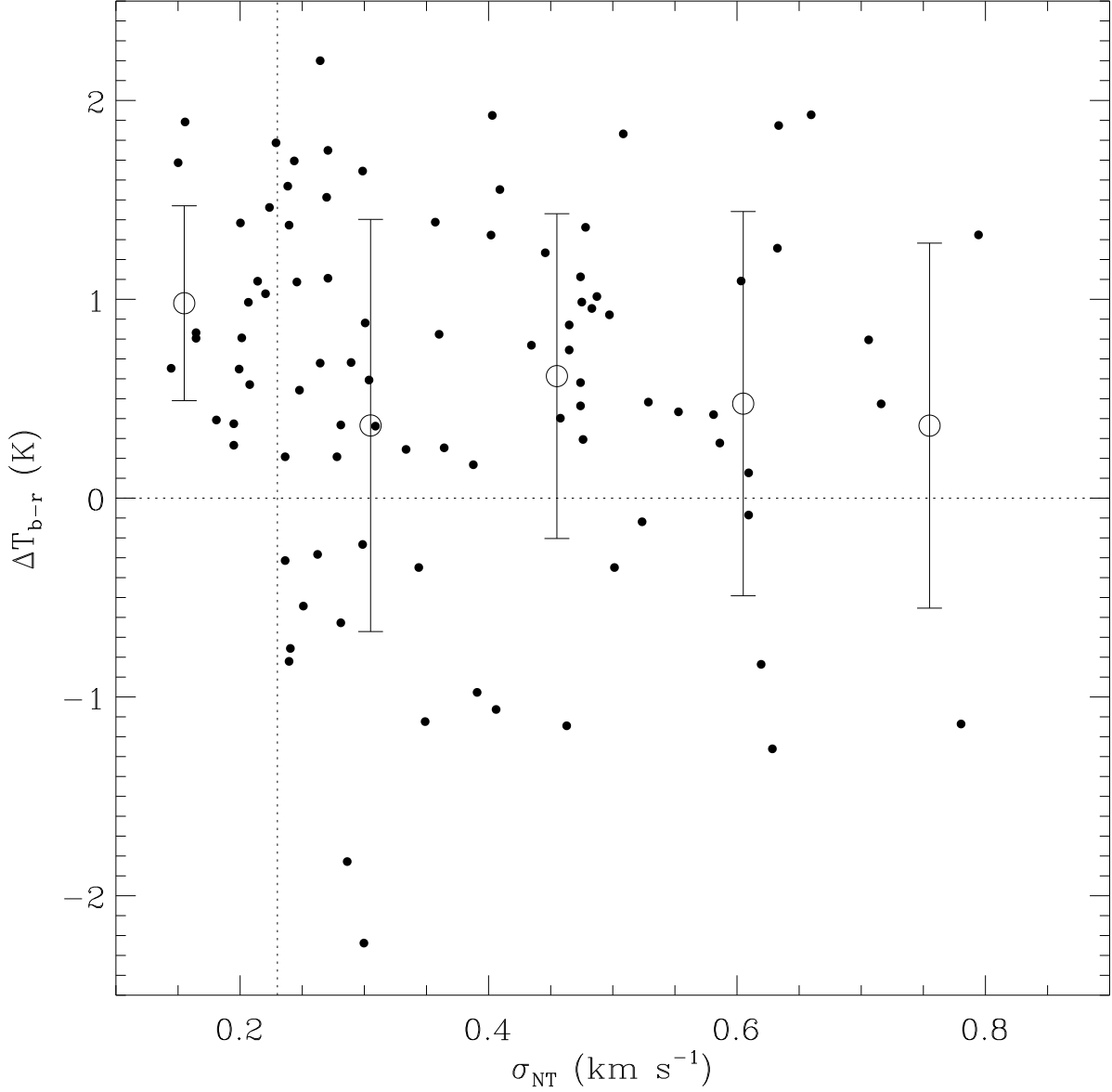


Fig. 8.— The CS blue-red temperature difference plotted against the N_2H^+ non-thermal velocity dispersion for all points in the dataset where both the CS spectra possess two peaks and the N_2H^+ spectra have a peak signal-to-noise ratio greater than 5. The vertical dotted line is drawn at $\sigma_{NT} = 0.23 \text{ km s}^{-1}$. All spectra with lower values of dispersion have positive values of ΔT_{b-r} indicating a positive infall speed. The large open circles and error bars indicate the mean and standard deviation of the temperature difference for five velocity dispersion bins.

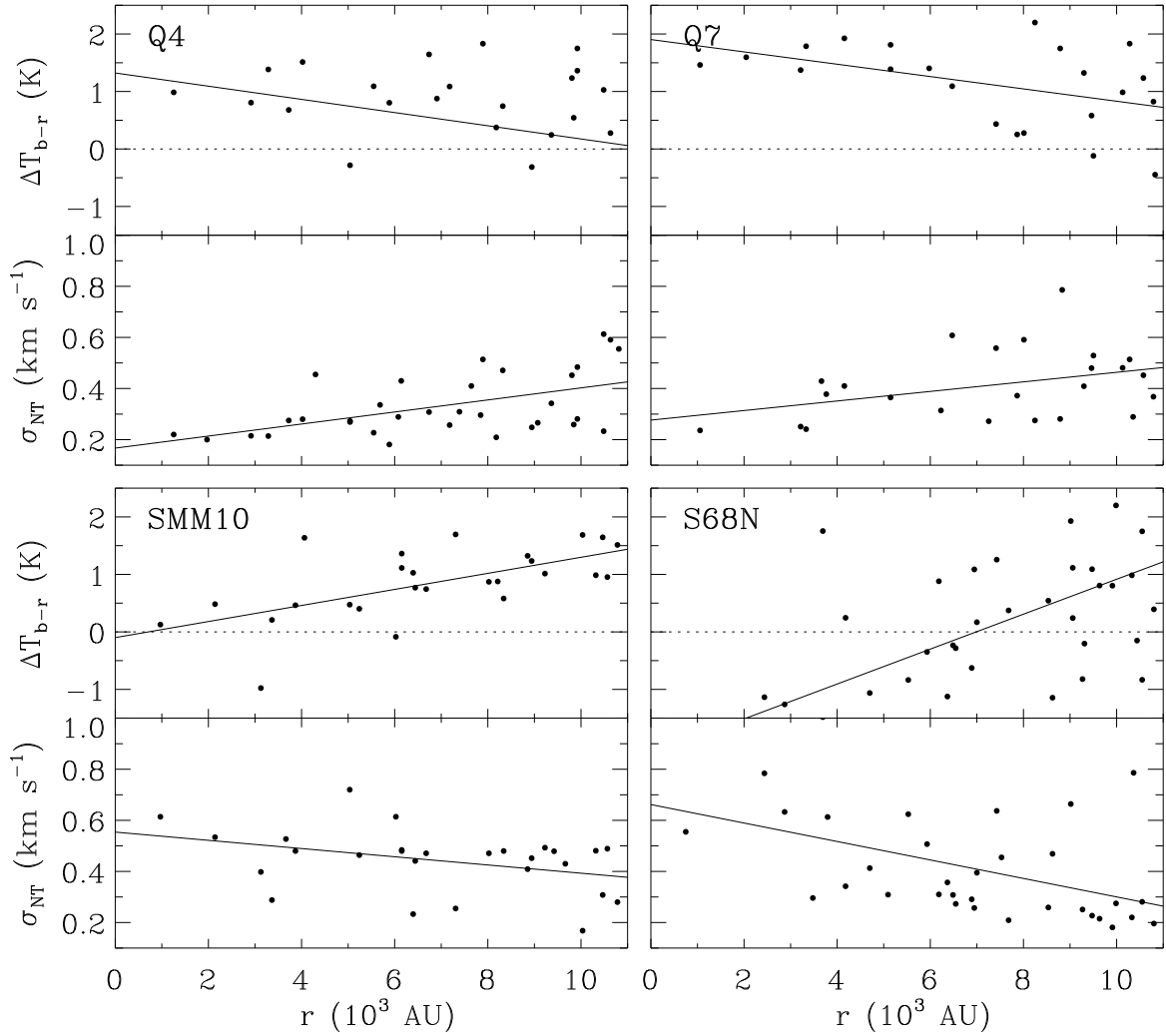


Fig. 9.— The radial variation of the CS blue-red temperature difference and N_2H^+ non-thermal velocity dispersion for two quiescent cores and two continuum sources. Points from individual spectra and a least squares fit are shown.

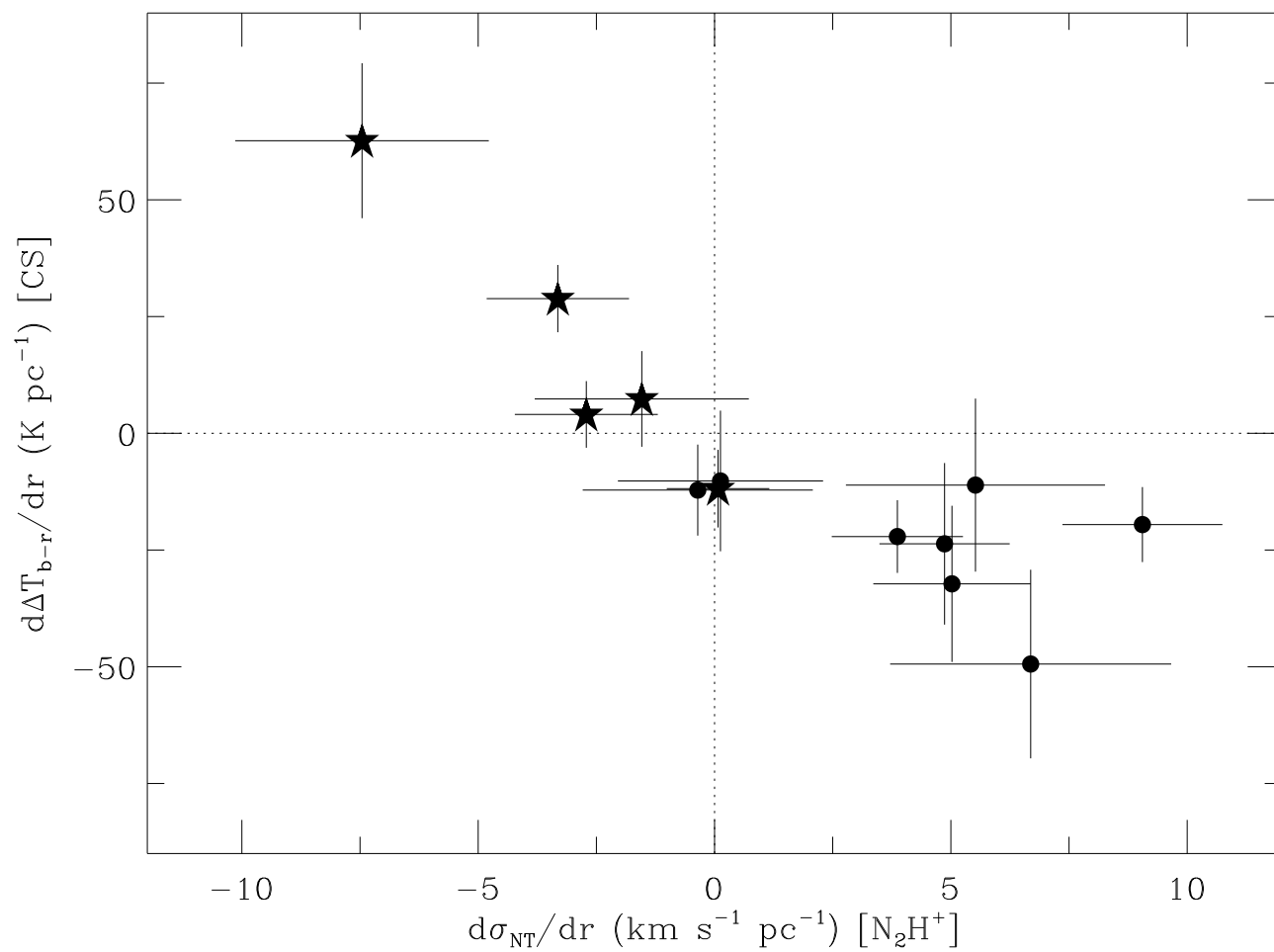


Fig. 10.— The radial gradient of $\Delta T_{\text{b-r}}(\text{CS})$ plotted against the radial gradient of $\sigma_{\text{NT}}(\text{N}_2\text{H}^+)$ for the continuum sources (stars) and quiescent cores (circles). The gradients are the slopes of least squares fits as in Figure 9.